Distribution and evolution of low-energy twin boundary density in time−space domain during isothermal compression for Ni80A superalloy

Jiang ZHAO[1], Guo-zheng QUAN[1,2], Yu-qing ZHANG[1], Wei XIONG[3]

1. Chongqing Key Laboratory of Advanced Mold Intelligent Manufacturing,
College of Materials Science and Engineering, Chongqing University, Chongqing 400044, China;
2. State Key Laboratory of Materials Processing and Die & Mould Technology,
Huazhong University of Science and Technology, Wuhan 430074, China;
3. Collaborative Innovation Center of Advanced Nuclear Energy Technology,
Key Laboratory of Advanced Reactor Engineering and Safety of Ministry of Education,
Institute of Nuclear and New Energy Technology, Tsinghua University, Beijing 100084, China

Abstract: Adjusting the density of low-energy boundary, i.e., $\Sigma 3^n$ twin boundary, in a thermal-plastic deformation process is a significant approach to enhance grain boundary-related properties for an alloy. In order to uncover the distribution and evolution of twin boundary density in a current-heating forming process, and their inner mechanisms dependent on grain size and stored-energy, an electrical−thermal−mechanical multi-field coupling and macro-micro multi-scale coupling finite element model was established. Simulation results of isothermal compression processes for Ni80A superalloy show that twin-boundary density keeps constant in the heating and holding stages, while it increases quickly and then intends to decrease in the compressing stage. Its distribution gets more homogeneous under high temperature and medium strain rate. The processing parameter domains corresponding to finer grain size and higher stored-energy, as well as higher dynamic recrystallization degree, contribute to promoting the twin boundary density.

Key words: $\Sigma 3^n$ twin boundary; multi-scale coupling simulation; current-heating forming; nickel-based superalloy

1 Introduction

Ni80A superalloy, as a typical nickel-based heat-resistance alloy with low stacking fault energy, has been widely used in the components of marine diesel engines and advanced gas turbine engines in virtue of its excellent comprehensive properties such as high strength, superior corrosion resistance and great creep-strength [1−3]. These components generally work in elevated temperature and strong corrosive conditions [4]. Such extreme service environments put forward a higher demand on the comprehensive properties of this alloy [5]. Traditional method for improving the comprehensive properties of an alloy is to obtain the grain refinement micro-structures induced by dynamic recrystallization (DRX) [2,6]. Nevertheless, grain refinement may reduce the ductility and the high-temperature creep property of alloys [7,8]. Grain boundary engineering (GBE) whose purpose is to manipulate the grain boundary character distribution (GBCD) of alloys, provides a solution [9]. According to GBE, there exist some special boundaries, often denoted as $\Sigma 3^n$ (n=1, 2, 3) twin boundaries, in the microstructures of alloys with low and medium stacking fault energy. High proportion of low-energy boundaries can effectively improve the boundary-related properties of an alloy [10−12]. It is worth noting that the Ni80A components are

usually manufactured by thermal forming processes, such as electric upsetting and die forging [13,14]. Therefore, it is quite meaningful to study the distribution and evolution of twin boundary density during the thermal-plastic deformation of Ni80A superalloy, and even identify the optimized thermal deformation conditions for acquiring higher twin boundary density.

Hitherto, there have been many studies on describing the evolution behaviors of twin boundaries during the thermal-plastic deformation processes of nickel-based alloys. AZARBARMAS et al [15] investigated the twin boundary evolution in a hot deformation process of Inconel 718 alloy, and found that the formation of twins is promoted by DRX process. BOZZOLO et al [16] studied the twin density evolution during a hot torsion process of a nickel-based alloy, and the results suggested that twin boundary density decreases with increasing grain size and decreasing grain boundary velocity. PRADHAN et al [17] elaborated the influence of thermal processing parameters on twin boundary evolution during the thermal deformation process of 617 alloy, and found that the rapid migration of high-angle boundaries is not always favorable to twin boundaries. JIANG et al [18] analyzed the evolution of twin boundaries in a low strain rate hot deformation for 617B alloy, and the results showed that $\Sigma 3^n$ boundaries are sensitively influenced by deformation temperature. From these studies, it can be concluded that the twin boundary density is governed by the synergistic effects of DRX, grain growth and twin formation, and all these mechanisms are sensitively dependent on the thermal-processing parameters including temperature, strain and strain rate [19−21]. A widely accepted fact is that the distributions of temperature, strain and strain rate on billet are generally uneven in a certain thermal deformation process. Thereupon, the distribution of twin boundary density is accordingly uneven and dynamically changeable in time−space domain. It is exceedingly difficult to track or directly observe the distribution and evolution of twin boundary density in a thermal deformation process of an alloy. Finite element method (FEM) is suitable for solving this problem.

The kinetic equations for describing the twin boundary density evolution are essential to construct the FEM model. In the past, a number of scholars developed various models to characterize the twin density evolution. GLEITER [22] built an atomic model to predict the twin density in an annealing process of Ni−Al alloy. PANDE et al [23] reviewed Gleiter's model, and proposed a semi-empirical model to characterize the evolution of twin boundary density in the process of grain growth. CAHOON et al [24] modified Pande's model by accounting for the influence of prior strain on the formation of twin boundaries in a commercially pure nickel. However, these models are established based on the static evolution process of twin boundary density. In our recent work [25], a physical model was developed to predict the twin boundary density during the thermal-plastic deformation process of Ni80A superalloy. In this model, twin boundary density is considered as the function of stored-energy and grain size, and the stored-energy can be calculated by average grain size and thermal deformation parameters. In the works of QUAN et al [26,27], the grain size evolution during the thermal deformation of Ni80A superalloy has been quantitatively evaluated using Johnson−Mehl−Avrami−Kolmogorov equation and Sellar model. Hence, the final kinetic equations can be formed by combining the grain size evolution models with the twin boundary density model.

In this work, an electrical−thermal−mechanical multi-field coupling and macro-micro multi-scale coupling FEM model was developed to uncover the distribution and evolution of $\Sigma 3^n$ boundary density during the isothermal compression process of Ni80A superalloy. The optimized deformation parameter domains, and their corresponding mechanisms for improving the twin boundary density were identified. The established FEM model was validated by EBSD characterization.

2 Experimental

The studied material is Ni80A superalloy whose chemical compositions (wt.%) are as follows: Cr 20.87, Ti 2.070, Fe 1.260, Al 0.680, Mn 0.630, Si 0.550, C 0.069, S 0.001 and balanced Ni. Six standard cylindrical specimens with 10 mm in diameter and 12 mm in height were separated from an as-forged Ni80A bar. Five of them were used for isothermal compression experiments and the remaining one was prepared for the characterization of the initial microstructures. The isothermal

compression experiments were carried out at a constant deformation temperature of 1100 °C and a strain rate of 0.1 s⁻¹ on a Gleeble−3500 thermal mechanical simulator. The experimental procedures can be schematically illustrated as Fig. 1. Firstly, the specimen was heated to 1100 °C at a heating rate of 5 °C/s, and held at that temperature for 3 min. Then, it was isothermally compressed to a specified height reduction with the strain rate of 0.1 s⁻¹, followed by water quenching. Here, the height reductions of the compression specimens were designated as 20%, 30%, 40%, 50% and 60%, corresponding to the true strains of 0.223, 0.357, 0.511, 0.693 and 0.916, respectively.
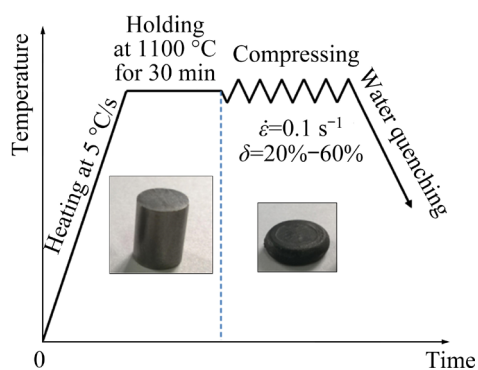

Fig. 1 Experimental procedures of isothermal compression process

After the isothermal compression, both the deformed specimens and the original one were sectioned in half along their axes. The cutting surfaces of the specimens were ground firstly, and then electro-polished in an electrolyte consisting of 10% $HClO_4$, 10% CH_3COOH and water at an electrolytic voltage of 20 V for 22 s. The central regions of the sectioned specimens were characterized using electron back scattered diffraction (EBSD) technology. And the collected EBSD data were post-processed by Oxford Instrument Channel 5 software, in which $\Sigma 3^n$ boundaries were identified based on Brandon criterion [28]. The critical angles for distinguishing the low-angle grain boundary (LAGB) and high-angle grain boundary (HAGB) were set as 2° and 15°, respectively. Grain size is determined based on the regions bounded by HAGBs. The grain orientation spread (GOS) criterion in classifying DRX grain, sub-grain and deformed grain is as follows [29]. If the average orientation within a grain is higher than the critical angle of

LAGB (2°), this grain will be identified as a deformed grain. If the average orientation within a grain is lower than 2°, and the misorientation between two adjacent regions surrounded by LAGBs exceeds 2°, this grain will be identified as a sub-grain. The rest are identified as DRX grains. For the purpose of quantitatively describing the content of $\Sigma 3^n$ twin boundaries in microstructures, the indicator of boundary length density ($BLD_{\Sigma 3^n}$, μm^{-1}), i.e., the length of $\Sigma 3^n$ twin boundaries per unit area, was introduced [30]. It can be calculated from EBSD maps by $(N_p \cdot \Delta)/A$, where N_p is the number of map-pixels representing $\Sigma 3^n$ twin boundaries, Δ is the scanning step size, and A is the area of observing window.

Initial microstructures of this alloy are characterized as Fig. 2. From the orientation imaging map in Fig. 2(a), it can be found that there are no obvious textures in the initial microstructures. Figure 2(b) shows the EBSD map of initial microstructures, in which HAGBs, LAGBs, $\Sigma 3$, $\Sigma 9$ and $\Sigma 27$ boundaries are highlighted by black, light-gray, red, green and purple lines, respectively.
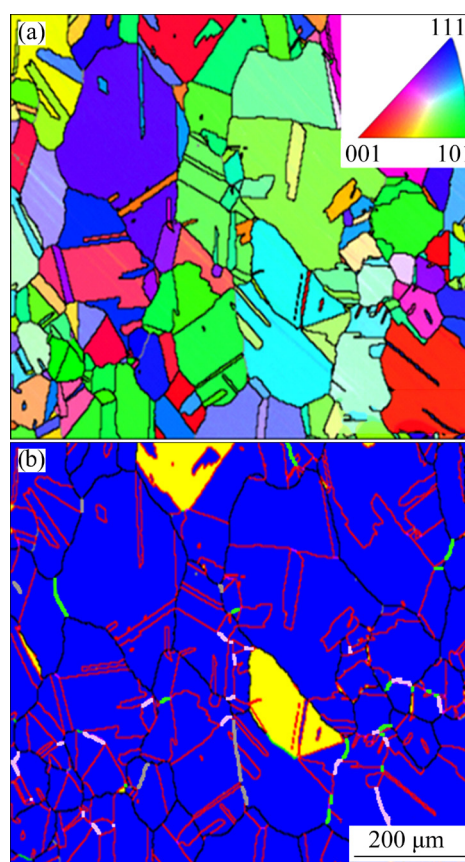
Fig. 2 Initial microstructures of studied alloy: (a) Orientation imaging map; (b) EBSD map with $\Sigma 3^n$ twin boundaries

DRX grain, sub-grain and deformed grain are marked in blue, yellow and red, respectively. From Fig. 2(b), it is noticeable that the initial microstructures consist of abundant equiaxed DRX grains and a small amount of sub-grains. The grain boundaries are relatively smooth, indicating that the stored strain energy is small. The average grain size was measured to be 34.8 μm, and the initial twin boundary density was calculated to be 0.0027 μm^{-1}.

3 FEM model describing twin-boundary density evolution

It is well known that the isothermal compression process is essentially a combinational issue of resistance heating and thermal-plastic deformation, in which the specimen is heated to an elevated temperature by direct current and then deformed under the thermal–mechanical coupling effects. For the evolution of $\Sigma 3^n$ twin boundary density, it depends on the variation of grain size and stored-energy, and all these variables can be calculated from three basic thermal deformation parameters (temperature, strain and strain rate) [25]. Thereupon, the isothermal compression FEM simulation for $\Sigma 3^n$ twin boundary density evolution can be summarized as two issues, i.e., electrical–thermal–mechanical multi-field coupling method and macro-micro multi-scale coupling analysis.

3.1 Electric–thermal–mechanical coupling analysis method

As mentioned above, the FEM simulation of isothermal compression process needs to consider the coupling effects of electric–thermal–mechanical multi-fields. Generally, such simulation process can be performed on some typical FEM solving platforms, such as MSC.marc, Abaqus, and Deform. During an electric–thermal–mechanical coupling analysis, the temperature field can be regarded as an intermediate variable to link the electric–thermal coupling module to the thermal–mechanical coupling module. For the electric−thermal coupling analysis, current density is calculated by Ohm's law, and the heat generated by resistance heating can be calculated by Joule's law. The temperature field obtained from the electric–thermal coupling analysis will be passed to the thermal–mechanical coupling module to solve the plastic deformation of billet. During the thermal–mechanical coupling

analysis, classic dynamic equilibrium equations are employed to calculate the rigid displacement and plastic flow of materials. Friction, plastic work and heat transfer among objects are considered. Furthermore, the temperature dependence of material parameters including electric resistivity, conductivity and heat-transfer coefficients is taken into account as well. The matrix equations used in the electric−thermal−mechanical coupling analysis are summed up as Eq. (1) [31]:

$$\begin{cases} \boldsymbol{Q}^{\mathrm{E}} = \boldsymbol{V}\boldsymbol{I} \\ \boldsymbol{K}^{\mathrm{E}}(T)\boldsymbol{V} = \boldsymbol{I} \\ \boldsymbol{M}\ddot{u} + \boldsymbol{D}\dot{u} + \boldsymbol{K}^{\mathrm{M}}(T,u,t)u = \boldsymbol{F} + \boldsymbol{F}^{\mathrm{T}} \\ \boldsymbol{C}^{\mathrm{T}}(T)\dot{T} + \boldsymbol{K}^{\mathrm{T}}(T)T = \boldsymbol{Q}^{\mathrm{T}} + \boldsymbol{Q}^{\mathrm{E}} + \boldsymbol{Q}^{\mathrm{I}} + \boldsymbol{Q}^{\mathrm{F}} \end{cases} \quad (1)$$

where $\boldsymbol{Q}^{\mathrm{E}}$ represents the Joule heat matrix. $\boldsymbol{V}$ and $\boldsymbol{I}$ represent the matrices of nodal voltage and current, respectively. $\boldsymbol{K}^{\mathrm{E}}(T)$ represents temperature-dependent electric conductivity matrix. $\boldsymbol{M}$ represents the mass matrix. $\boldsymbol{D}$ is the damping coefficient matrix. $\boldsymbol{K}^{\mathrm{M}}(T, u, t)$ represents the stiffness matrix, which is the function of temperature T, node-displacement u and time t. $\boldsymbol{F}$ represents the loading external force. $\boldsymbol{F}^{\mathrm{T}}$ represents the thermal stress resulting from uneven temperature distribution. $\boldsymbol{C}^{\mathrm{T}}(T)$ is the temperature-related heat capacity coefficient matrix. $\boldsymbol{K}^{\mathrm{T}}(T)$ represents the temperature-dependent heat-transfer coefficient matrix. $\boldsymbol{Q}^{\mathrm{T}}$, $\boldsymbol{Q}^{\mathrm{I}}$ and $\boldsymbol{Q}^{\mathrm{F}}$ represent the heat flux matrices resulting from heat transfer, plastic work and friction, respectively.

For a certain isothermal compression FEM simulation, the electric field, temperature field and mechanical field will be solved in sequence, and the flow chart for the solution process is shown in Fig. 3. Based on the electric–thermal–mechanical coupling analysis algorithm, the distribution and evolution of various macro indicators including voltage, current density, temperature, energy density, displacement, strain, strain rate and stress can be obtained.

3.2 Macro-micro multi-scale coupling analysis method

In order to simulate the distribution and evolution of $\Sigma 3^n$ twin boundary density, the kinetic model incorporating the evolution of twin boundary density is essential. According to our previous work [25], for the thermal-plastic deformation process of Ni80A superalloy, twin boundary density
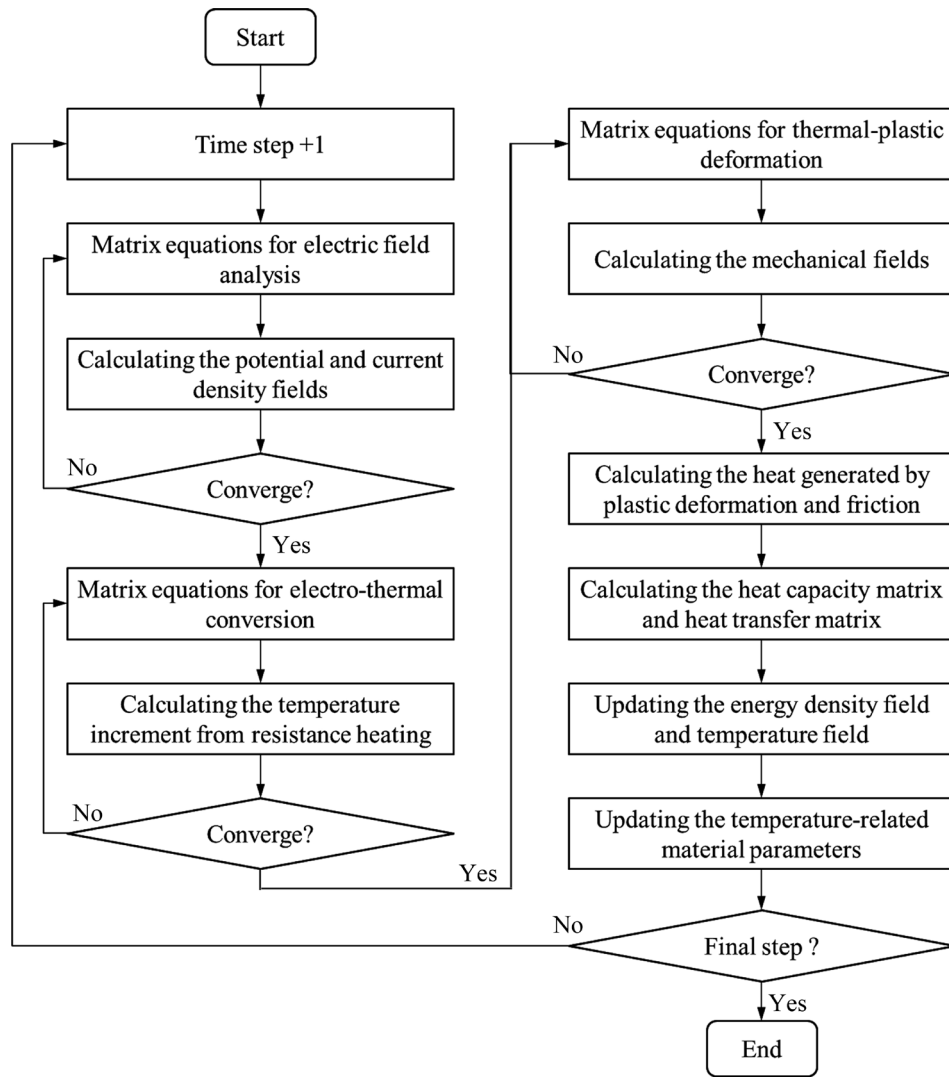
Fig. 3 Flow chart of electric−thermal−mechanical coupling analysis

($BLD_{\Sigma 3^n}$) can be expressed as the function of grain size and stored-energy, as shown in Eq. (2):

$$BLD_{\Sigma 3^n} = \frac{\pi}{2} k_1 \frac{(1+k_2 E_s)}{\bar{D}} \ln\left(\frac{\bar{D}}{D_0}\right) \qquad (2)$$

where $\bar{D}$ represents the average grain size, D_0 represents the critical grain size, below which $\Sigma 3^n$ twin boundaries will not be generated, E_s represents the stored-energy, and k_1 and k_2 are coefficients.

During the thermal-plastic deformation process of an alloy, grain size is governed by the comprehensive functions of DRX and grain growth mechanisms. In the work of QUAN et al [26], the DRX behaviors of Ni80A superalloy were investigated, and an Avrami-type equation was established and successfully implanted into an FEM software platform to simulate the evolution process of DRX volume fraction. The formula of DRX

kinetics can be shown as follows:

$$X_{drx} = 1 - \exp\left[-\beta_d \left(\frac{\varepsilon - \varepsilon_c}{\varepsilon_{0.5}}\right)^{k_d}\right] \qquad (3)$$

where X_{drx} represents the DRX volume fraction. Both k_d and β_d are coefficients. ε_c represents the critical strain, below which DRX will not happen. $\varepsilon_{0.5}$ represents the strain corresponding to the DRX volume fraction of 50%, and it can be evaluated by Eq. (4):

$$\varepsilon_{0.5} = a\dot{\varepsilon}^m \exp[Q/(RT)] \qquad (4)$$

where a is a coefficient. m is the strain rate sensitivity exponent. $\dot{\varepsilon}$ is the strain rate. R represents the molar gas constant. Q is the deformation activation energy at $\varepsilon_{0.5}$. As for the critical strain ε_c, it is proportional to the peak strain (ε_p), as shown in Eq. (5):

$$\varepsilon_c = \alpha_1 \varepsilon_p \tag{5}$$

where a_1 is a coefficient. The peak strain under different deformation temperatures and strain rates can be calculated by Eq. (6):

$$\varepsilon_p = a_2 \dot{\varepsilon}^{m_1} \exp[Q_1/(RT)] \tag{6}$$

where a_2 is a coefficient. m_1 is the strain rate sensitivity exponent. Q_1 is the deformation activation energy at peak strain. Moreover, the DRX grains size (D_{drx}) can be evaluated by Eq. (7):

$$D_{drx} = a_3 d_0^h \varepsilon^n \dot{\varepsilon}^{m_2} \exp[Q_2/(RT)] \tag{7}$$

where a_3 is a coefficient. m_2, n and h are the exponents of strain rate, strain and initial grain size, respectively. Q_2 is the activation energy for DRX. d_0 represents the initial grain size. Then, the average grain size can be evaluated by Eq. (8) [26]:

$$\bar{D} = d_0(1-X_{drx}) + D_{drx}X_{drx} \tag{8}$$

It must be noted that the effect of grain growth is considerable during the thermal deformation process of Ni80A superalloy. Here, the increase of grain size resulting from grain growth mechanism for Ni80A superalloy can be evaluated by Sellar model, as shown in Eq. (9) [27]:

$$d^{m_3} = d_1^{m_3} + a_4 t \exp[-Q_3/(RT)] \tag{9}$$

where d represents the grain size growth and d_1 represents the grain size before it grows up. m_3 and a_4 are coefficients. Q_3 is the activation energy of grain growth.

As for the stored-energy E_s, it can be calculated by Eq. (10) [25], in which n_1 is the grain size exponent. Both c_1 and c_2 are coefficients, varying with thermal deformation parameters.

$$E_s = \frac{c_1}{\bar{D}^{2n_1}} \ln\left(\frac{\bar{D}^{n_1}}{c_2}\right) \tag{10}$$

The solving process and values of the coefficients in Eqs. (2)−(10) are indicated in our previous works [25−27]. To sum up, based on the above mathematical models including twin-boundary density evolution, DRX kinetics and grain growth, the microstructural indicators including grain size, DRX volume fraction, stored-energy and twin-boundary density can be calculated. Finally, all of these equations were implanted into an electric-thermal−mechanical multi-field coupling FEM model, so as to conduct macro-micro coupling analysis. The flow chart for macro-micro coupling analysis is shown in Fig. 4.

3.3 Isothermal compression FEM model

Combining the electric−thermal−mechanical coupling method with the macro-micro coupling
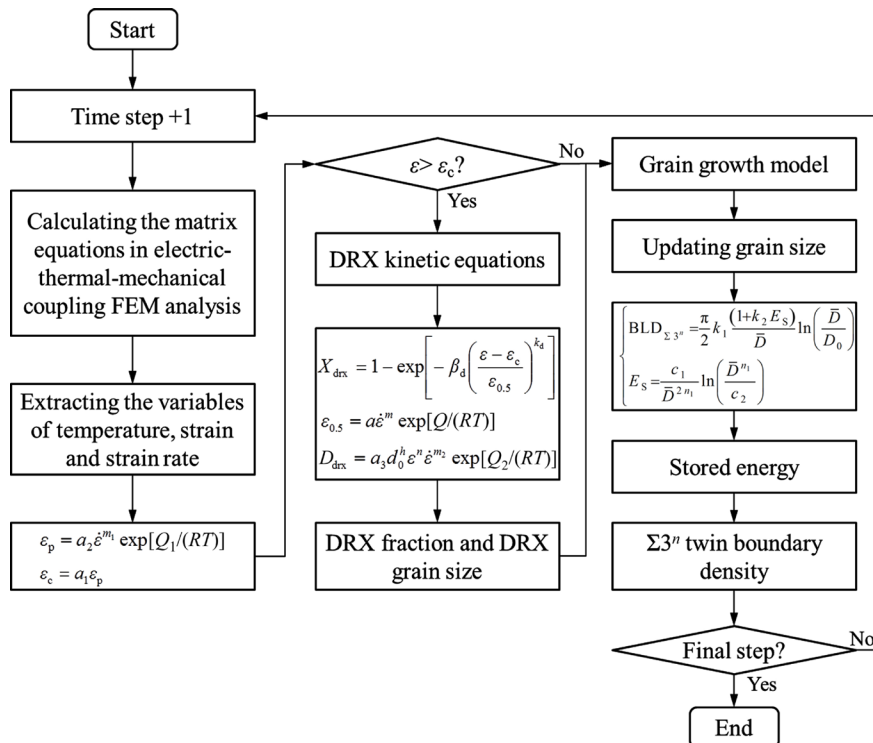

Fig. 4 Flow chart for macro-micro coupling analysis

analysis procedures, a two-dimensional and half-symmetry isothermal compression FEM model was established. Planar four-node quadrilateral element was applied to meshing the cylindrical specimen and anvils. The geometry and mesh of the isothermal compression FEM model are presented in Fig. 5. Four points ($P1$, $P2$, $P3$ and $P4$) on the central axis of the specimen were selected as the sampling sites for analyzing the evolution process of various indicators. The lower anvil in pink was defined as a fixed rigid body, while the upper anvil in yellow was set as a mobile part with a definable velocity (v). Current density, i.e., current intensity per unit area (A/mm^2), was loaded on the end surface of the upper anvil. The end surface of the lower anvil was defined as zero potential. Initial temperatures of the specimen and anvils were set as room temperature (20 °C). Heat radiation coefficients of the anvils and specimen were set as 0.02. Considering the actual lubrication condition in the isothermal compression experiments, the friction coefficients between specimen and anvils were specified as 0.3. The stress−strain data of Ni80A superalloy were obtained from our previous work [26].
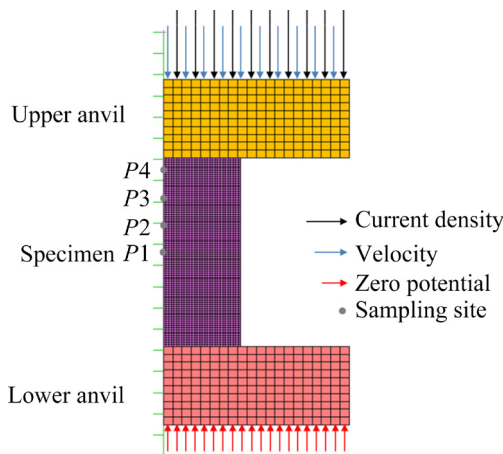

Fig. 5 FEM model of isothermal compression process

In order to simulate the real isothermal compression process, the current loading needs to be designed carefully. After repeated attempts, the current loading paths corresponding to different temperatures (1000−1150 °C) for the heating and holding processes were designed and shown in Fig. 6. For the compression process, the designed current loading paths are exhibited in Fig. 7.

To ensure the relatively constant strain rate in isothermal compression process, the velocity of upper anvil needs to be planned. Here, a conversion relationship between strain rate ($\dot{\varepsilon}$) and compressing velocity (v) is shown in Eq. (11), by which the loading path of anvil velocity corresponding to each constant strain rate can be designed [26]. Taking the strain rate of 0.1 s^{-1} as an example, the planned upper anvil velocity is shown in Fig. 8.

$$v = h_0 \dot{\varepsilon} \exp(-\dot{\varepsilon} t) \tag{11}$$

where h_0 represents the original height of the isothermal compression specimen, and t is the duration time of compression process.
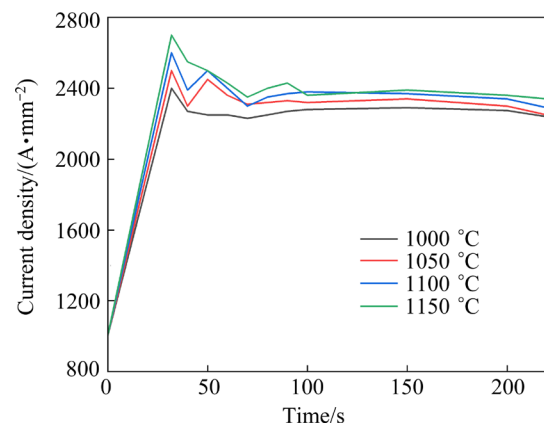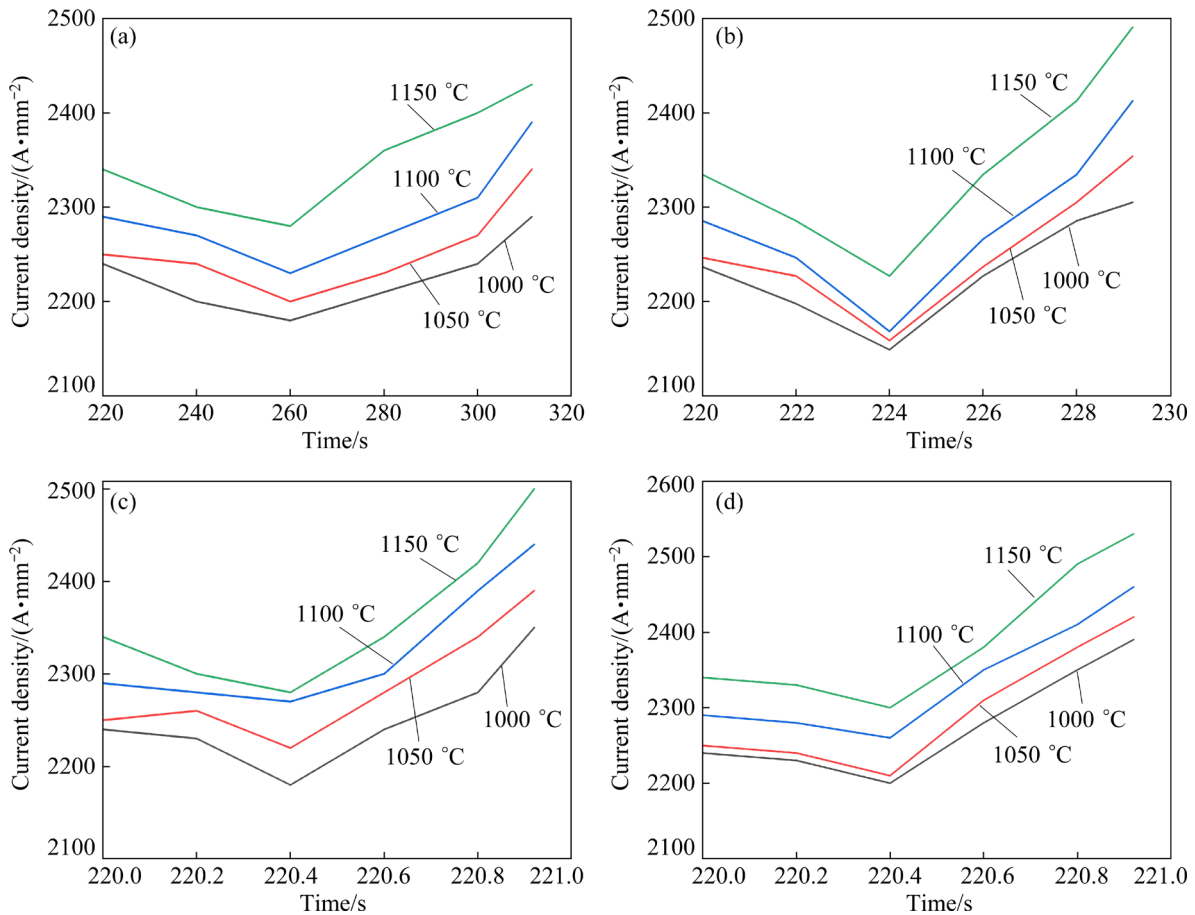

**Fig. 6** Designed current loading paths for heating and holding processes

4 Results and discussion

4.1 Distribution and evolution of grain size in time−space domain

Based on the established FEM model, for the deformation condition of 1100 °C and 0.1 s^{-1}, the grain size distribution and evolution in different stages of isothermal compression process are illustrated in Fig. 9. In Fig. 9(a), the nephograms (a') and (b') represent the grain size distributions at the end of heating and holding stages, respectively. It can be seen from Fig. 9(a) that due to the short heating time, grain growth is not provoked completely at the heating stage, while the effect of grain growth is remarkable at the holding stage. Additionally, the grain size distribution is inhomogeneous and the larger grain size appears in the center of the specimen because of the relatively high temperature existing in the interior of the specimen. According to Fig. 9(b), at the compressing stage, DRX occurs and grain size is refined accordingly. The grain size in the center of

Fig. 7 Designed current loading paths for compression process at different temperatures and strain rates: (a) 0.01 s^{-1}; (b) 0.1 s^{-1}; (c) 1 s^{-1}; (d) 10 s^{-1}
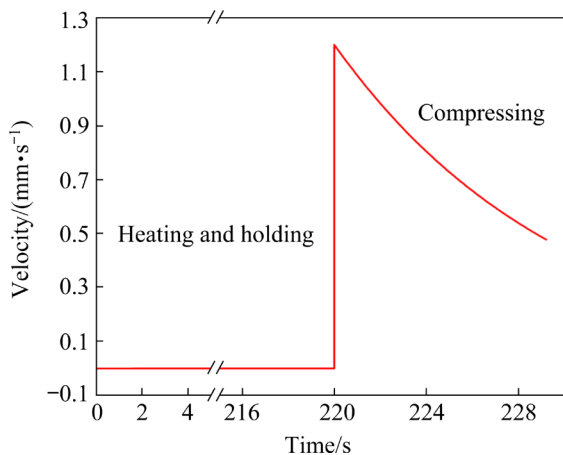
**Fig. 8** Velocity of upper anvil at strain rate of 0.1 s^{-1}

the specimen is finer owing to the higher DRX degree where the plastic deformation is more sufficient.

In order to analyze the influence of deformation conditions on grain size evolution, the final grain size distributions of the specimens deformed under different isothermal compression conditions are presented in Fig. 10. An apparently

similar feature in these grain size distributions is that the finer grain size appears in the central region of the specimens. Besides, it seems that the fine-grain region gets larger with increasing temperature and strain rate. Reasons for this phenomenon are as follows. When the specimen is deformed under a higher deformation temperature, most material of the specimen will be yielded and deformed. Accordingly, the plastic deformation in specimen is more sufficient, thereby promoting the DRX process and enlarging the fine-grain region. On the other hand, the lower strain rate is generally favorable for coordinating the uneven plastic deformation in specimens. Therefore, the more homogeneous grain size distributions can be obtained under lower strain rates. From the nephograms of grain size distribution, it is found that the fine-grain region becomes smaller at the lower strain rate.

To better describe the influence of deformation parameters on grain size evolution, the values of grain size and DRX volume fraction at sampling
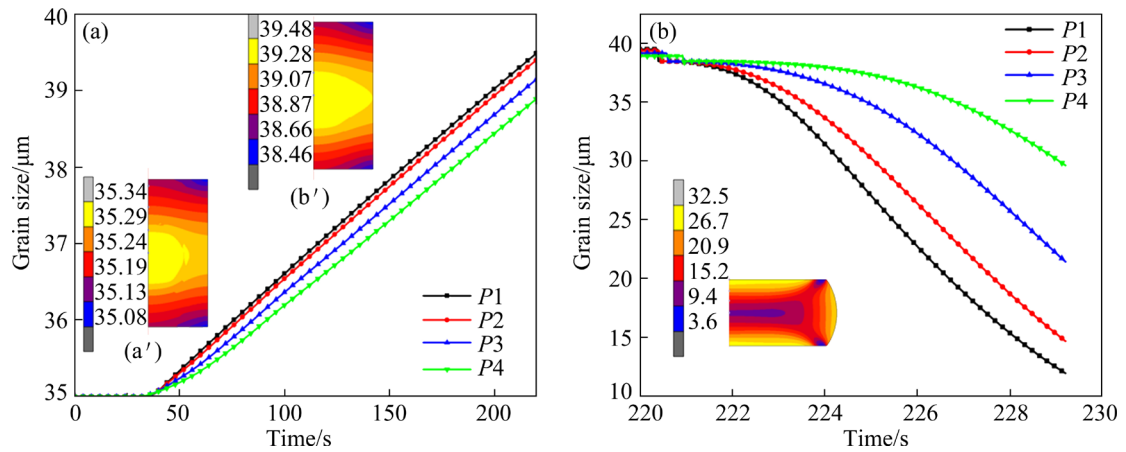
Fig. 9 Distribution and evolution of grain size at heating and holding (a) and compressing (b) stages of isothermal compression process at 1100 °C and 0.1 s⁻¹
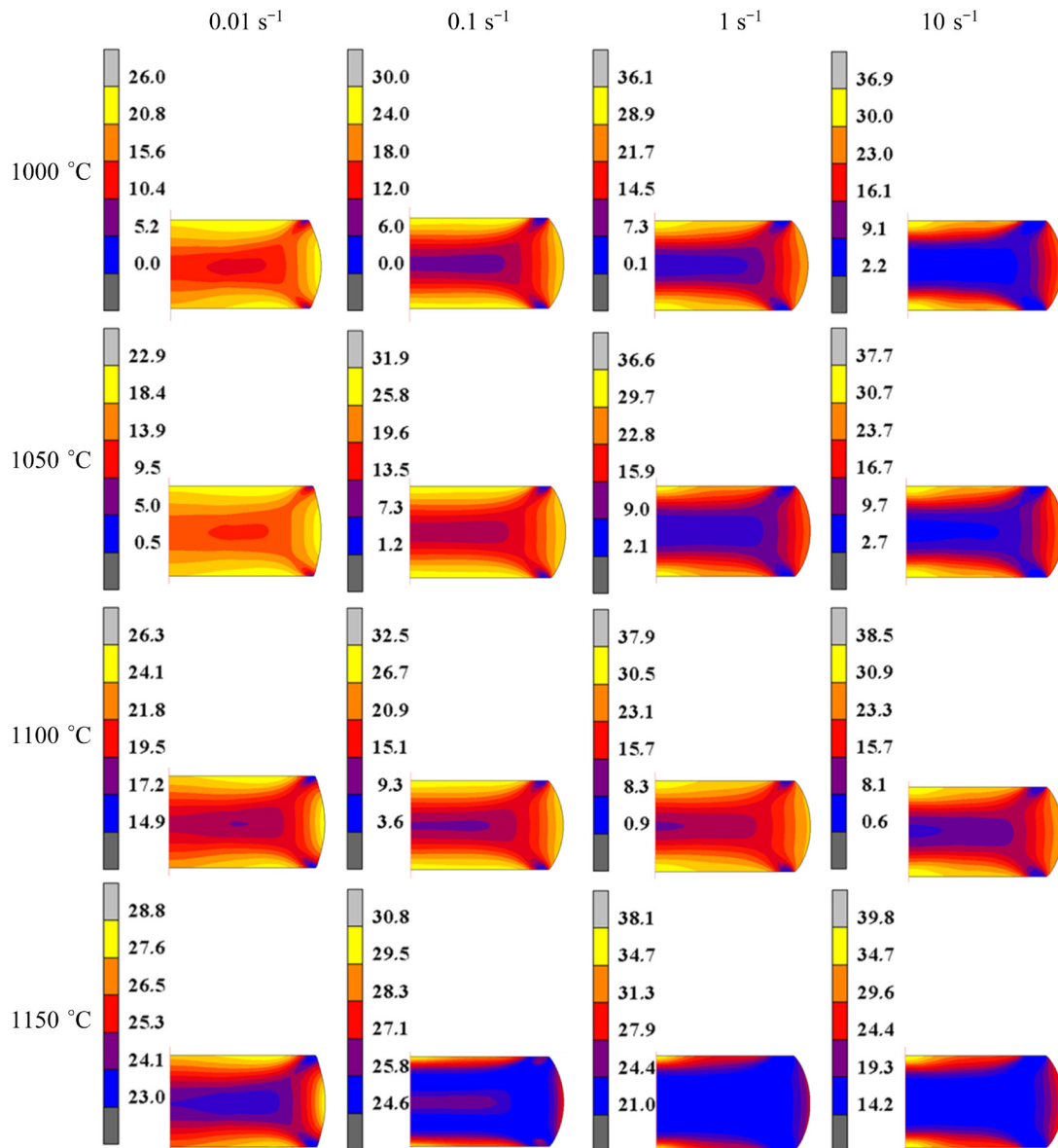
Fig. 10 Grain size distributions at end of isothermal compression process under diverse isothermal compression conditions (Unit: μm)

point $P1$ of the specimens were extracted, and their variations with temperature and strain rate are plotted in Figs. 11(a) and (b), respectively. It can be seen from Fig. 11(a) that grain size decreases with increasing strain rate and decreasing temperature. According to Fig. 11(b), DRX volume fraction is remarkably higher at high temperature and low strain rate. It is well known that DRX is a thermal activated process. Higher deformation temperature contributes to promoting the nucleation and growth of DRX grains. Lower strain rate can provide enough time for the occurrence of DRX process. That's why the higher DRX fraction intends to appear at higher temperature and lower strain rate. It is worth noting that the effect of grain growth mechanism will be weak when the specimen is deformed at low temperature [32]. The tangles and intersections among dislocations will be intensified at high strain rate, which is favorable for the nucleation of DRX grains [33]. Because of the high nucleation rate of DRX grains and low grain growth velocity under higher strain rate and lower temperature, the finer grain size is obtained.

As the isothermal compression experiments of Ni80A superalloy over the studied deformation parameters have been done in our previous work [25], the grain size distribution (Fig. 11(a)) and DRX volume fraction distribution (Fig. 11(b)) can be verified. The average relative error between simulated grain size and experimental one was evaluated as 11.4%, which indicates that the simulated grain size is reliable. In addition, the variations of grain size and DRX volume fraction with processing parameters are in good agreement with the experiment results obtained in our previous work [25].
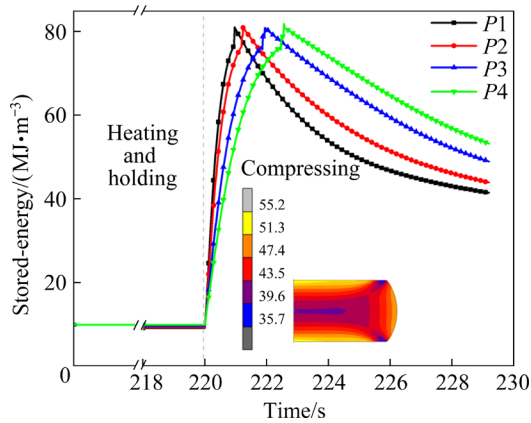
4.2 Distribution and evolution of stored-energy in time−space domain

As twin boundary density depends not only on grain size, but also on stored-energy, it is essential to reveal the distribution and evolution of stored-energy during the isothermal compression process of Ni80A superalloy. Figure 12 shows the evolution and distribution of stored-energy in spacial and temporal domains at the deformation temperature of 1100 °C and the strain rate of 0.1 s^{-1}. Clearly, the stored-energy basically remains constant during the heating and holding stages, while it increases rapidly until the peak in the early stage of the compressing process, and then it decreases slowly with further increasing strain. Moreover, it can be noted from Fig. 12 that the stored-energy in the central region of the specimen reaches its maximum earlier, and decreases at a faster rate. The final stored-energy distribution is inhomogeneous, and the higher stored-energy values appear in the near surface regions of the specimen. A widely accepted fact is that stored-energy is directly determined by dislocation density [34], and the variation of stored-energy is affected by various mechanisms including work hardening (WH), DRX, dynamic recovery (DRV) and grain growth. At the heating and holding stages, DRV and grain growth are dominant, therefore, the dislocation density intends to decrease. In view of the initial microstructures composed of dislocation-free grains, the stored-energy always keeps in a low
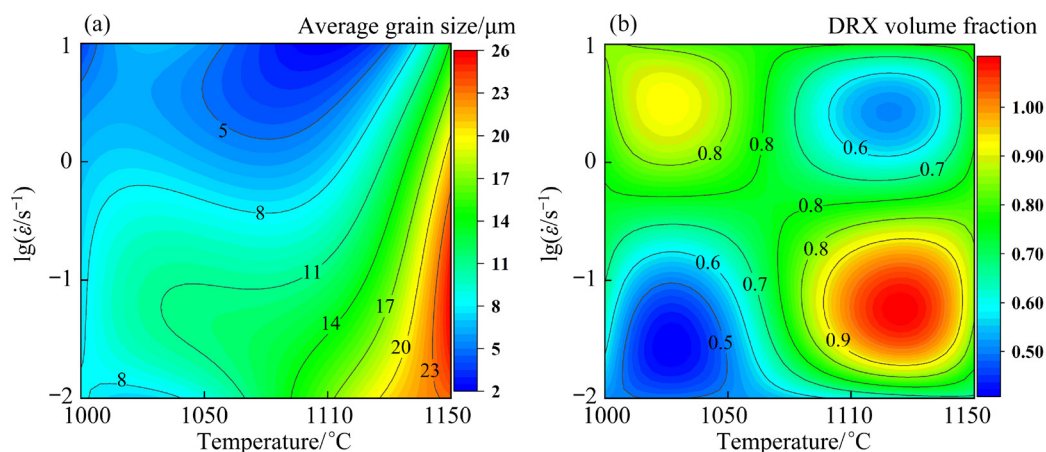
Fig. 11 Variations of grain size (a) and DRX volume fraction (b) at sampling site $P1$ for specimen deformed at various temperatures and strain rates
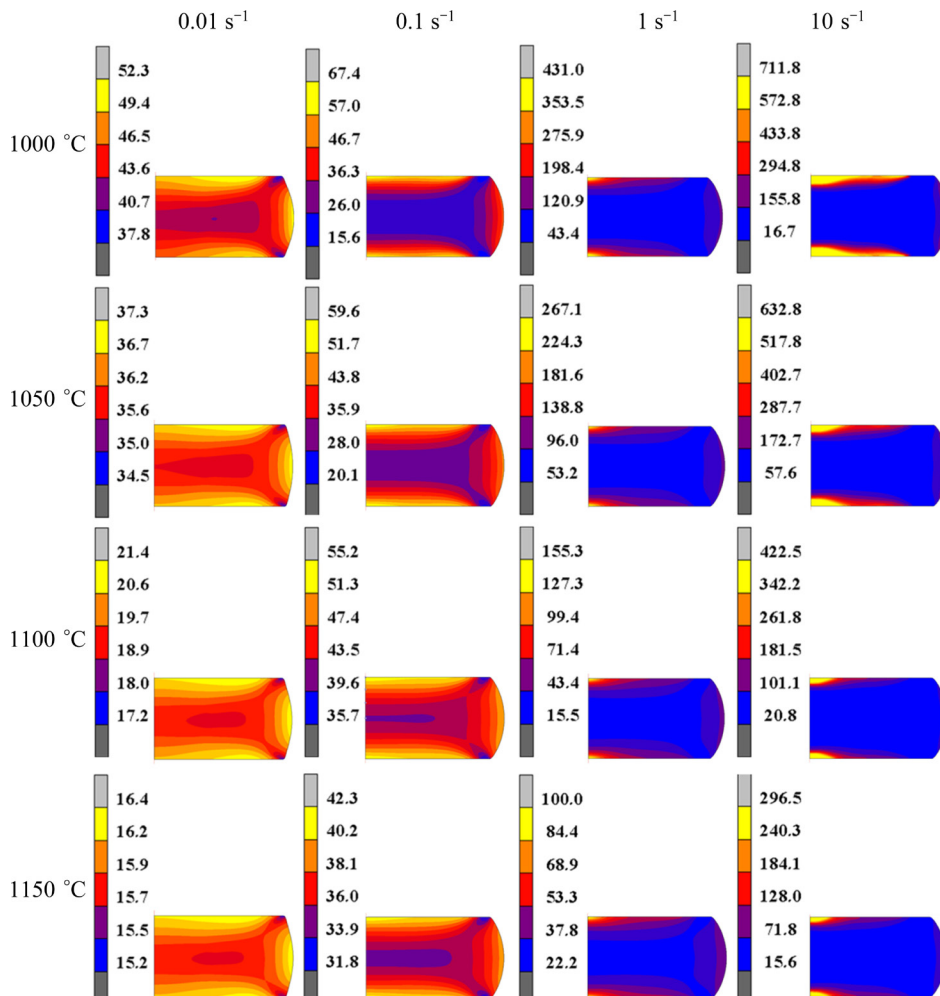
Fig. 12 Distribution and evolution of stored-energy during isothermal compression process at 1100 °C and 0.1 s^{-1}

level at the heating and holding stages. In the compressing stage, dislocation density first increases due to WH, and then decreases with the occurrence of DRX process. Accordingly, the stored-energy increases firstly and then decreases slowly.

Figure 13 illustrates the final stored-energy distribution of the specimens deformed under different isothermal compression conditions. According to Fig. 13, it can be found that the stored-energy distribution varies widely under different deformation conditions. Here, for the purpose of assessing the distribution characteristics of stored-energy, the indicator standard deviation (SD), which represents the heterogeneity of stored-energy distribution, is introduced. It can be calculated by Eq. (12).

$$SD = \frac{1}{n}\sum_{i=1}^{n}(\theta_i - \theta_{av})^2 \tag{12}$$

where θ_i represents the average value of stored-energy for any element, θ_{av} represents the average value of stored-energy in the billet, and n is the number of billet elements. The SD-values under diverse thermal deformation conditions were figured out, and the results are shown in Table 1. From Table 1, it is apparently seen that the stored-

Fig. 13 Spacial distribution of stored-energy at end of isothermal compression process under different deformation conditions (Unit: MJ/m^3)

Table 1 SD-values of stored-energy for specimens deformed under different conditions

Temperature/ °C	SD/(MJ·m⁻³)			
	0.01 s⁻¹	0.1 s⁻¹	1 s⁻¹	10 s⁻¹
1000	2.54	6.48	28.26	87.73
1050	1.16	5.57	20.53	72.87
1100	0.40	3.48	13.90	60.08
1150	0.20	3.20	8.26	35.15

energy distribution becomes more and more homogeneous with increasing the deformation temperature and decreasing strain rate. These phenomena may be caused by the following reasons. Firstly, the higher temperature is beneficial to reducing the deformation resistance of alloy, which makes the plastic deformation of specimens more homogeneous. Secondly, plastic deformation can be coordinated well under lower strain rates because there is enough time for the grain rotation and slip system activating. In addition, the material near the surface of specimen can be heated to an elevated deformation temperature when the specimen is deformed at a low strain rate and a high temperature, which expands the impact range of DRX and makes the stored-energy distribution more homogeneous on the specimen.
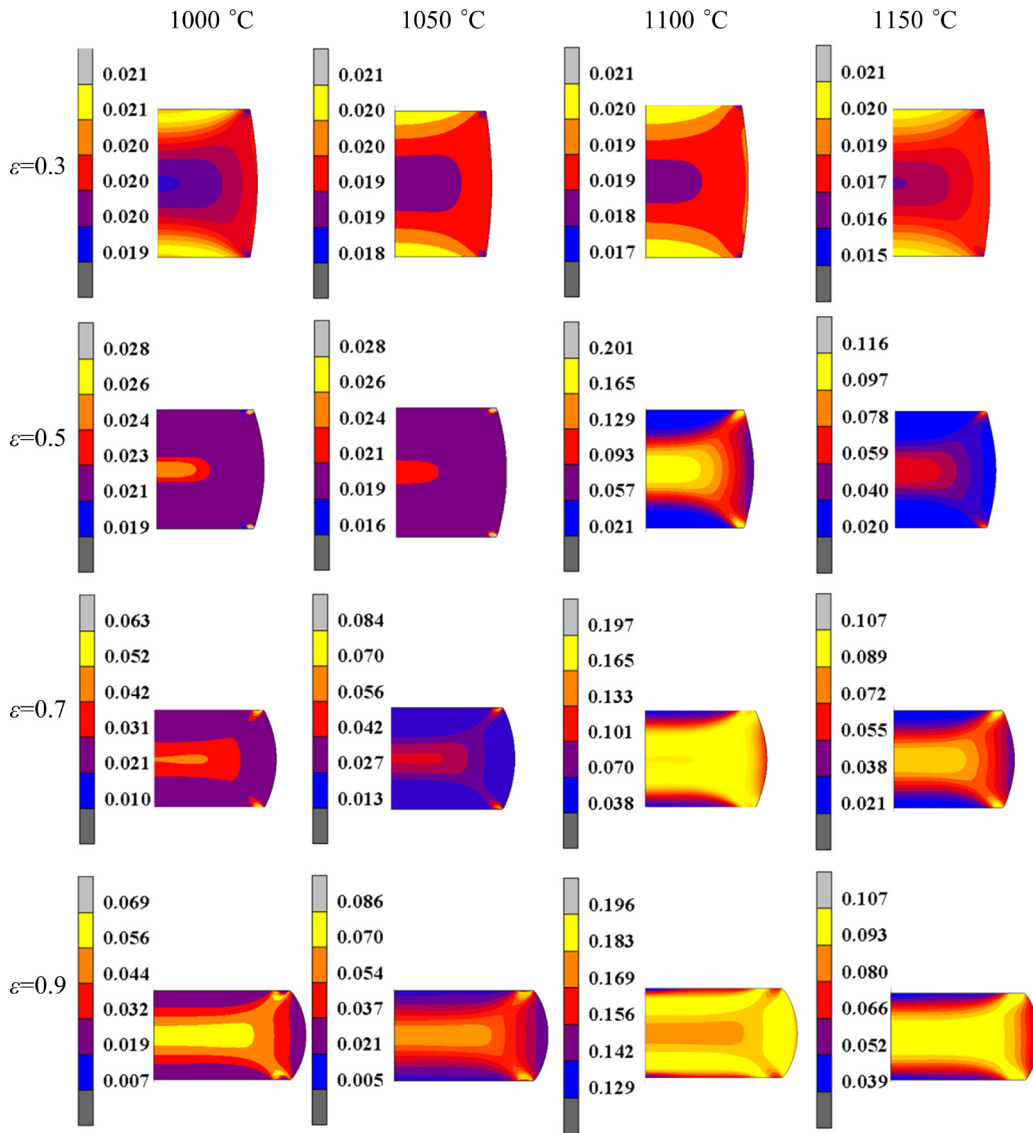
4.3 Distribution and evolution of twin boundary density in time−space domain

The distribution and evolution of twin boundary density at deformation temperature of 1100 °C and strain rate of 0.1 s⁻¹ are obtained based on FEM simulation, and the numerical results are shown in Fig. 14. Similar to the trend of stored-energy, twin boundary density keeps roughly constant in the heating and holding stages on the ground of the slightly increasing grain size and basically constant stored-energy. At the compressing stage, twin boundary density increases firstly and then decreases after it reaches the peak. The reasons accounting for the variation tendency of twin boundary density are as follows. During the isothermal compression process, when the plastic strain exceeds the critical value of DRX onset, abundant DRX grains nucleate and grow up. The possibility of stalking fault increases in virtue of the rapid grain boundary migration during the growth of new-born DRX grains [22,23,35]. Thereupon, twin boundary density increases significantly

along with the continuously increasing DRX degree. With the further increasing compression strain, stored-energy is heavily consumed (Fig. 12), and the driving force for grain boundary migration decreases correspondingly [36]. More importantly, the space for grain growth is limited because most original grains have been replaced by refined DRX grains. Therefore, the twin boundary density intends to decrease at the later stage of DRX process.
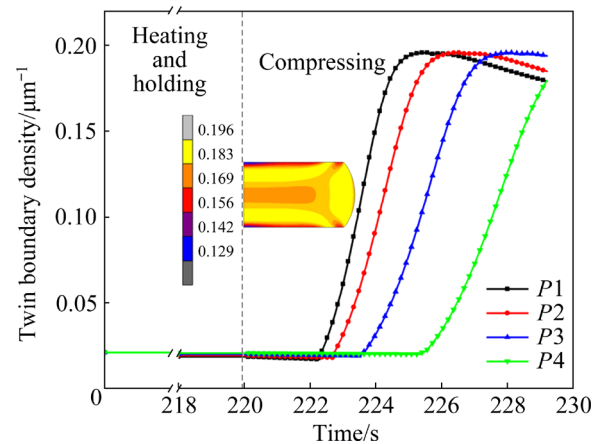
Fig. 14 Distribution and evolution of twin boundary density during isothermal compression process at 1100 °C and 0.1 s⁻¹

In order to clarify the influence of temperature on the distribution and evolution of twin boundary density, the isothermal compression processes were simulated at different deformation temperatures and a constant strain rate. Since the twin boundary density keeps basically constant during the heating and holding stages, its evolution in the two stages will be ignored in the following discussion. Figure 15 reveals the distribution and evolution of twin boundary density in time−space domain for the specimens deformed at different temperatures and a constant strain rate of 0.1 s⁻¹. It is evident that with increasing temperature, the formation of twin boundaries is accelerated firstly and then delayed. At the lower deformation temperature, DRX process is retarded, which decreases the nucleation rate of twin boundaries [32]. On the other hand, the higher deformation temperature would lead to coarser grain size, thus also decreasing the twin boundary density [30]. Moreover, it can be observed from Fig. 15 that the region with higher twin boundary density changes under different deformation temperatures, and the twin density distribution is more homogeneous at higher
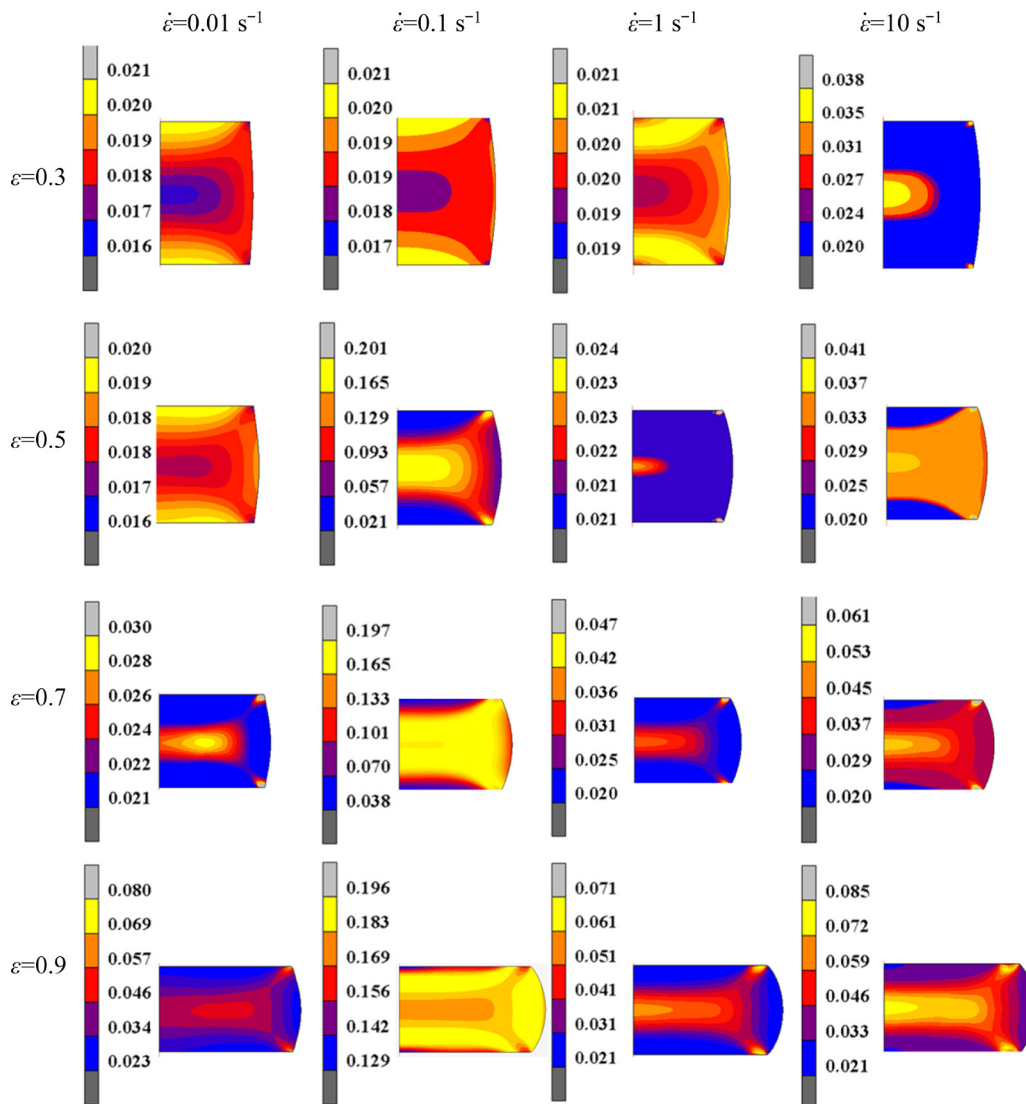
Fig. 15 Spacial and temporal distribution of twin boundary density in deformation temperature range of 1000−1150 °C at constant strain rate of 0.1 s^{-1} (Unit: μm^{-1})

temperatures. Reasons accounting for these results are as follows. It has been acknowledged that for the constant strain rate of 0.1 s^{-1}, DRX occurs more completely at higher temperatures, as shown in Fig. 11(b). The higher DRX degree contributes to forming twin boundaries. However, it must be mentioned that the DRX process will consume abundant stored-energy. At the later stage of DRX process, twin boundary density intends to decrease owing to the over-consumed stored-energy, as shown in Fig. 12. Accordingly, the twin boundary density in the central region of specimen begins to decrease (Fig. 14). Thus, the largest twin boundary density regions shift from the center of the specimen to the near edge regions of the specimen

with the further increasing compression strain. Meanwhile, the twin boundary density in the near edge regions of specimen keeps increasing at the compressing stage, and the difference of twin boundary density between the central and near edge regions becomes smaller with the proceeding of compression process. Consequently, the final twin boundary density distribution looks more homogeneous at the higher deformation temperatures.

Figure 16 reveals the spacial and temporal distribution of twin boundary density in isothermal compression process in the strain rate range of 0.01−10 s^{-1} at 1100 °C. It is apparent that the distribution of twin boundary density is complex under the varying strain rates. At the lower strain

Fig. 16 Spacial and temporal distribution of twin boundary density in strain rate range of 0.01−10 s^{-1} at 1100 °C (Unit: μm^{-1})

rate of 0.01 s^{-1}, the grain size is coarser (Fig. 11(a)) and the stored-energy is smaller (Fig. 13). Correspondingly, the twin boundary density is lower. As for the higher strain rates, the twin boundary density distribution is uneven and their values are lower. It can be attributed to the fact that the higher strain rate provides less time for the growth of DRX grains, thus decreasing the possibility of grain growth accident. More importantly, according to Table 1, the stored-energy distribution is extremely uneven when the specimen is deformed at higher strain rates. This is the main factor causing the uneven twin density distribution at higher strain rates. In a word, the distribution of twin boundary density is more homogeneous at medium strain rate.

Furthermore, the variations of twin boundary density at the sampling point $P1$ for the specimens deformed under diverse temperatures and strain rates were extracted and exhibited in Fig. 17. It is apparent that twin boundary density intends to increase with increasing true strain under all the studied isothermal compression conditions. Particularly, there are two favorable thermal processing-parameter windows, i.e., 1075−1125 °C, 0.032−0.316 s^{-1} and 1000−1050 °C, 1−10 s^{-1}, where the twin boundary densities are obviously higher. And the mechanisms underlying the two windows are different. For the window of 1000−1050 °C and 1−10 s^{-1}, finer grain size and higher stored-energy are obtained, as shown in Figs. 11(a) and 13. It has been proven that the finer
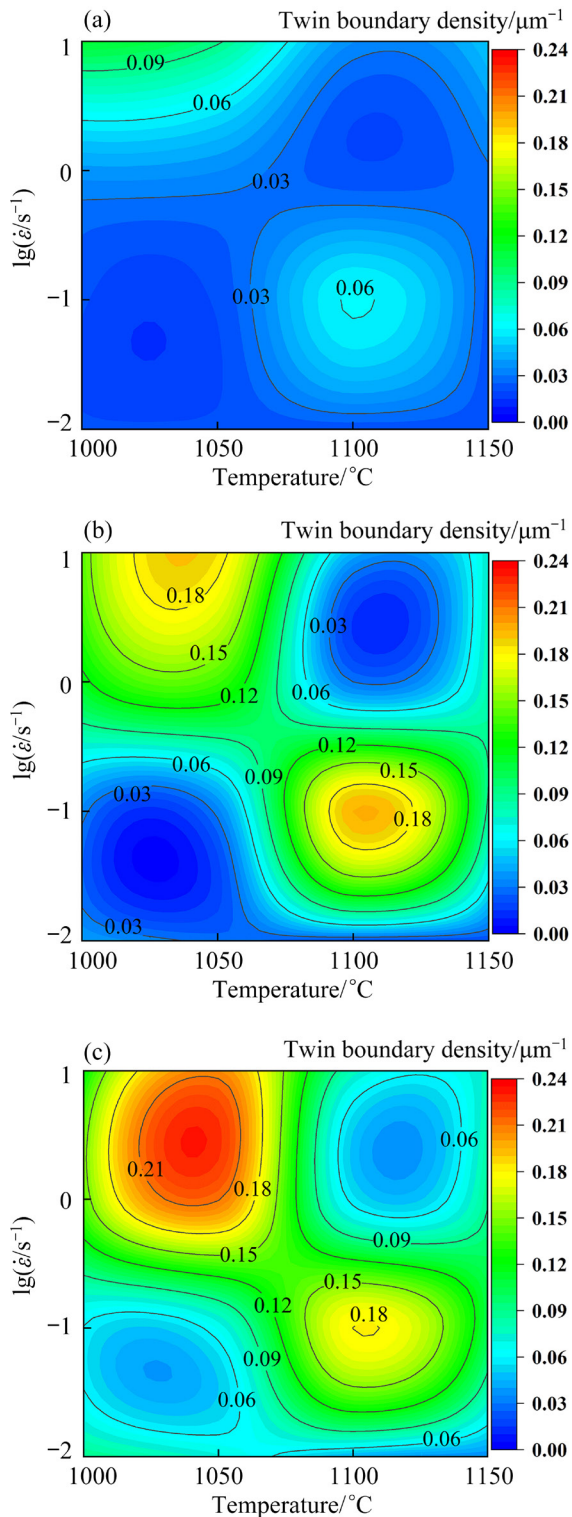
Fig. 17 Variations of twin boundary density with temperature and strain rate at different true strains: (a) 0.3; (b) 0.6; (c) 0.9

grain size can effectively promote the twin formation in DRX process [16,30]. The higher stored-energy represents stronger driving force for grain boundary migration, which can accelerate the

nucleation and growth of twin boundaries [36,37]. As for the other window of 1075−1125 °C and 0.032−0.316 s⁻¹, the DRX volume fraction is remarkably higher according to Fig. 11(b). Besides, the power dissipation maps of Ni80A superalloy achieved from our previous work also proved that the DRX occurs more easily under the mentioned thermal deformation domains [6]. Therefore, the higher twin boundary density was obtained under this condition because of higher DRX degree.

5 Validation based on microstructure characterization

In order to validate the reliability of the established FEM model, microstructures of the specimens deformed at 1100 °C and 0.1 s⁻¹ with different height reductions were characterized, and the results are shown in Fig. 18. When the specimen was compressed to the height reduction of 20%, the original grains were elongated and the twin boundary fraction was still relatively low, as shown in Figs. 18(a, a'). With increasing the plastic strain, the initial grains were gradually refined due to the occurrence of DRX, as shown in Figs. 18(b−e) and (b'−e'). In addition, it can be noticed from Figs. 18(b−e) and (b'−e') that the fraction of $\Sigma 3$ twin boundaries got higher with the proceeding of compression process. And the fraction of $\Sigma 9$ and $\Sigma 27$ twin boundaries also increased with increasing the plastic strain. There is a widely acknowledged fact that the twin boundaries can interact with each other and lead to "multiple twining" phenomenon when the twin boundary density exceeds a threshold value [20]. The interactions among twin boundaries can be described in Eq. (13). That is to say, the formation of $\Sigma 3$, $\Sigma 9$ and $\Sigma 27$ twin boundaries can promote each other.

$$\begin{cases} \Sigma 3 + \Sigma 3 \rightarrow \Sigma 9 \\ \Sigma 3 + \Sigma 9 \rightarrow \Sigma 27 \\ \Sigma 9 + \Sigma 27 \rightarrow \Sigma 3 \end{cases} \quad (13)$$

To verify the simulated grain size and twin boundary density, the grain size values and the $\mathrm{BLD}_{\Sigma 3^n}$-values of these EBSD maps were counted and calculated, and both the experimental values and the simulated results were presented in Fig. 19. Figure 19(a) exhibited the comparison of grain size between simulated results and experimental ones. The average relative error of grain size in Fig. 19(a)
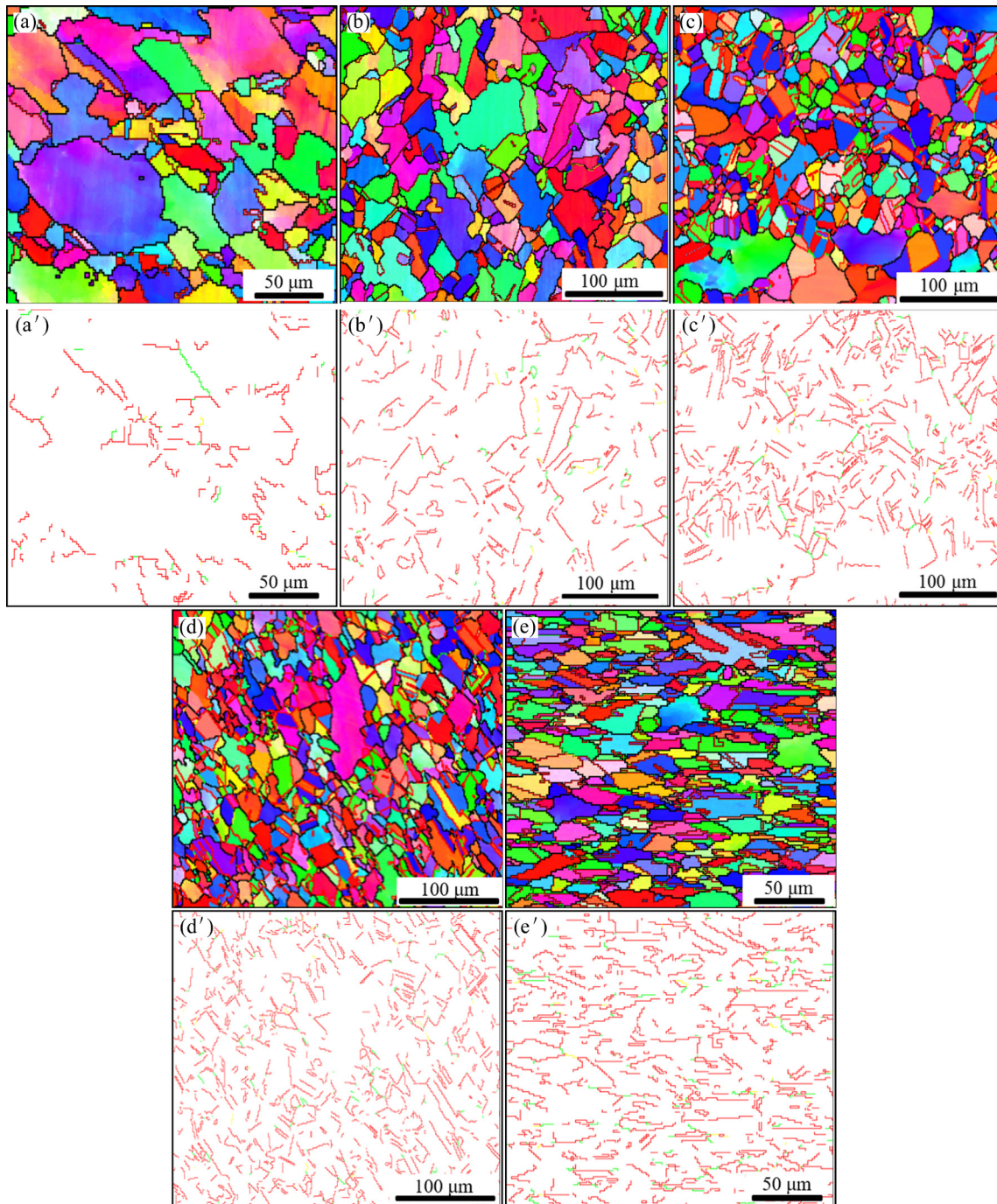
Fig. 18 Microstructures of specimens deformed at 1100 °C and 0.1 s^{-1} with different height reductions: (a, a') 20%; (b, b') 30%; (c, c') 40%; (d, d') 50%; (e, e') 60%

was evaluated as 5.03%, which indicates that the grain size model used in this work is credible. Figure 19(b) revealed the comparison of simulated twin densities with the measured ones. The nephograms in Fig. 19(b) showed the distributions of twin boundary density obtained from FEM simulation. It can be seen from Fig. 19(b) that the variation tendency of twin density obtained from

numerical simulation is in agreement with the experimental results. The average relative error between simulated twin boundary densities and the experimental ones was evaluated as 6.14%, which indicates that the established FEM model can well describe the evolution and distribution of twin boundary density during the isothermal compression process of Ni80A superalloy.
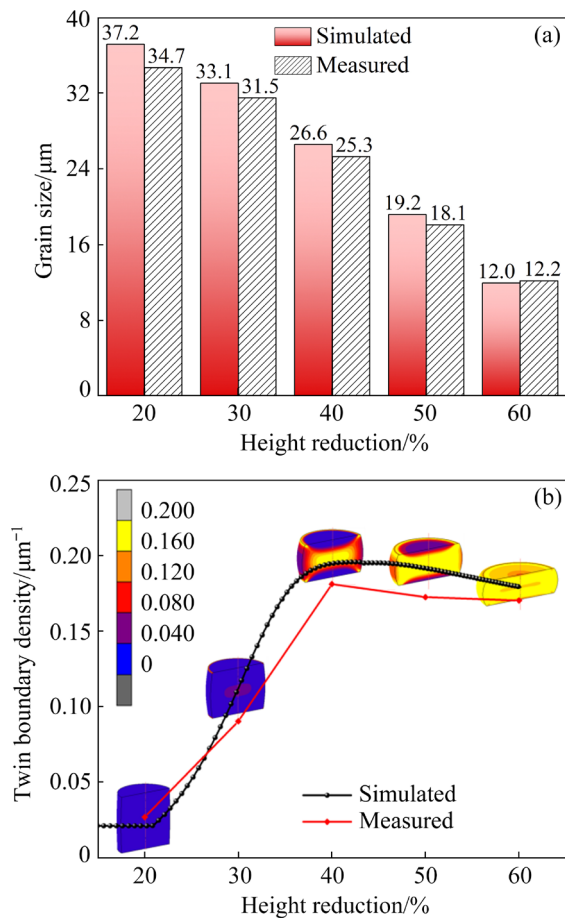
Fig. 19 Comparison of average grain size (a) and twin boundary density (b) between simulated results and experimental ones

6 Conclusions

(1) An electro−thermal−mechanical multi-field and macro-micro multi-scale coupling FEM model was established to unravel the distribution and evolution of twin boundary density in the current-heating forming process of Ni80A superalloy.

(2) During the heating and holding stages, the distribution of twin boundary density keeps basically unchanged because of the slowly increasing grain size and roughly-constant stored-energy. During the compressing stage, twin boundary density increases firstly, and then decreases owing to the over-reduced stored-energy. Besides, the distribution of twin boundary density is more homogeneous under higher deformation temperature and medium strain rate.

(3) Two favorable thermal processing parameter windows corresponding to higher twin boundary density were identified. One is 1000−1050 °C and 1−10 s^{-1}, where finer grain size and higher stored-energy are beneficial to the nucleation and growth of twin boundaries. The other is 1075−1125 °C and 0.032−0.316 s^{-1}, where higher DRX degree contributes to the formation of twin boundaries.

(4) The established FEM model was validated by microstructure characterization. The average relative error between simulated twin boundary densities and the experimental ones was evaluated as 6.14%, which indicates that the established FEM model can well describe the evolution and distribution of twin boundary density during the isothermal compression process of Ni80A superalloy.

References

[1]   KIM D K, KIM D Y, RYU S H, KIM D J. Application of Nimonic 80A to the hot forging of an exhaust valve head [J]. Journal of Materials Processing Technology, 2001, 113(1): 148−152.

[2]   ZHU Yuan-zhi, YIN Zhi-min, XU Jiang-pin. Microstructural mapping in closed die forging process of superalloy Nimonic 80a valve head [J]. Journal of Alloys and Compounds, 2011, 509(20): 6106−6112.

[3]   XU Yu-lai, YANG Cai-xiong, XIAO Xue-shan, CAO Xiu-li, JIA Guo-qing, SHEN Zhi. Evolution of microstructure and mechanical properties of Ti modified superalloy Nimonic 80A [J]. Materials Science and Engineering A, 2011, 530: 315−326.

[4]   POLLOCK T M, TIN S. Nickel-based superalloys for advanced turbine engines: Chemistry, microstructure and properties [J]. Journal of Propulsion and Power, 2006, 22: 361−374.

[5]   DETROIS M, GOETZ R L, HELMINK R C, TIN S. Modeling the effect of thermal-mechanical processing parameters on the density and length fraction of twin boundaries in Ni-base superalloy RR1000 [J]. Materials Science and Engineering A, 2015, 647: 157−162.

[6]   QUAN Guo-zheng, LIU Qiao, ZHAO Jiang, XIONG Wei, SHI Rui-ju. Determination of dynamic recrystallization parameter domains of Ni80A superalloy by enhanced processing maps [J]. Transactions of Nonferrous Metals Society of China, 2019, 29(7): 1449−1464.

[7]   SOULA A, RENOLLET Y, BOIVIN D, POUCHOU J L, LOCQ D, CARON P, BRÉCHET Y. Analysis of high-temperature creep deformation in a polycrystalline nickel-base superalloy [J]. Materials Science and Engineering A,

2009, 510/511: 301−306.

[8] BRIDGES D, XU R, HU A M. Microstructure and mechanical properties of Ni nanoparticle-bonded Inconel 718 [J]. Materials & Design, 2019, 174: 107784.

[9] TAN L, ALLEN T R, BUSBY J T. Grain boundary engineering for structure materials of nuclear reactors [J]. Journal of Nuclear Materials, 2013, 441(1/2/3): 661−666.

[10] TELANG A, GILL A S, TAMMANA D, WEN X S, KUMAR M, TEYSSEYRE S, MANNAVA S R, QIAN D, VASUDEVAN V K. Surface grain boundary engineering of Alloy 600 for improved resistance to stress corrosion cracking [J]. Materials Science and Engineering A, 2015, 648: 280−288.

[11] ATHREYA C N, DEEPAK K, KIM D I, de BOER B, MANDAL S, SARMA V S. Role of grain boundary engineered microstructure on high temperature steam oxidation behaviour of Ni-based superalloy alloy 617 [J]. Journal of Alloys and Compounds, 2019, 778: 224−233.

[12] PALUMBO G, AUST K T, ERB U, KING P J, BRENNENSTUHL A M, LICHTENBERGER P C. On annealing twins and CSL distributions in F.C.C. polycrystals [J]. Physica Status Solidi, 1992, 131: 425−428.

[13] BIBA N, LISHNIJ A, VLASOV A. Simulation of coupled problem of electric upsetting [J]. Journal of Materials Processing Technology, 1998, 80: 184−187.

[14] ZHANG Yu-qing, QUAN Guo-zheng, ZHAO Jiang, XIONG Wei. Influence of variable loading path pattern on deformation and grain size in large-scale electric upsetting process of Nimonic superalloy [J]. The International Journal of Advanced Manufacturing Technology, 2022, 120: 5933−5954.

[15] AZARBARMAS M, AGHAIE-KHAFRI M, CABRERA J M, CALVO J. Dynamic recrystallization mechanisms and twining evolution during hot deformation of Inconel 718 [J]. Materials Science and Engineering A, 2016, 678: 137−152.

[16] BOZZOLO N, SOUAÏ N, LOGÉ R E. Evolution of microstructure and twin density during thermomechanical processing in a γ−γ' nickel-based superalloy [J]. Acta Materialia, 2012, 60: 5056−5066.

[17] PRADHAN S K, MANDAL S, ATHREYA C N, BABU K A, de BOER B, SARMA V S. Influence of processing parameters on dynamic recrystallization and the associated annealing twin boundary evolution in a nickel base superalloy [J]. Materials Science and Engineering A, 2017, 700: 49−58.

[18] JIANG He, DONG Jian-xin, ZHANG Mai-cang, YAO Zhi-hao. Evolution of twins and substructures during low strain rate hot deformation and contribution to dynamic recrystallization in alloy 617B [J]. Materials Science and Engineering A, 2016, 649: 369−381.

[19] QIN Feng-ming, ZHU Hua, WANG Zhen-xing, ZHAO Xiao-dong, HE Wen-wu, CHEN Hui-qin. Dislocation and twinning mechanisms for dynamic recrystallization of as-cast Mn18Cr18N steel [J]. Materials Science and Engineering A, 2017, 684: 634−644.

[20] CHEN X M, LIN Y C, WU F. EBSD study of grain growth behavior and annealing twin evolution after full recrystallization in a nickel-based superalloy [J]. Journal of Alloys and Compounds, 2017, 724: 198−207.

[21] PRITHIV T S, BHUYAN P, PRADHAN S K, SARMA V S, MANDAL S. A critical evaluation on efficacy of recrystallization vs. strain induced boundary migration in achieving grain boundary engineered microstructure in a Ni-base superalloy [J]. Acta Materialia, 2018, 146: 187−201.

[22] GLEITER H. The formation of annealing twins [J]. Acta Materialia, 1969, 17(12): 1421−1428.

[23] PANDE C S, IMAM M A, RATH B B. Study of annealing twins in fcc metals and alloys [J]. Metallurgical Materials Transactions A, 1990, 21(11): 2891−2896.

[24] CAHOON J R, LI Q Y, RICHARDS N L. Microstructural and processing factors influencing the formation of annealing twins [J]. Materials Science and Engineering A, 2009, 526(1/2): 56−61.

[25] QUAN Guo-zheng, ZHANG Yu-qing, ZHANG Pu, MA Yao-yao, WANG Wei-yong. Correspondence between low-energy twin boundary density and thermal-plastic deformation parameters in nickel-based superalloy [J]. Transactions of Nonferrous Metals Society of China, 2021, 31(2): 438−455.

[26] QUAN Guo-zheng, LI Yong-le, ZHANG Le, WANG Xuan. Evolution of grain refinement degree induced by dynamic recrystallization for Nimonic 80A during hot compression process and its FEM analysis [J]. Vacuum, 2017, 139: 51−63.

[27] QUAN Guo-zheng, ZHANG Pu, MA Yao-yao, ZHANG Yu-qing, LU Chao-long, WANG Wei-yong. Characterization of grain growth behaviors by BP-ANN and Sellars models for nickle-base superalloy and their comparisons [J]. Transactions of Nonferrous Metals Society of China, 2020, 30(9): 2435−2448.

[28] BRANDON D G. The structure of high-angle grain boundaries [J]. Acta Materialia, 1966, 14(11): 1479−1484.

[29] JORGE B D, IZA M A, GUTIÉRREZ I. Evaluation of intragranular misorientation parameters measured by EBSD in a hot worked austenitic stainless steel [J]. Journal of Microscopy, 2010, 228(3): 373−383.

[30] SHI Hui, CHEN Ke, SHEN Zhi, WU Jie-qiong, DONG Xian-ping, ZHANG Lan-ting, SHAN Ai-dang. Twin boundary characters established during dynamic recrystallization in a nickel alloy [J]. Materials Characterization, 2015, 110: 52−59.

[31] QUAN Guo-zheng, PAN Jia, ZHANG Zhi-hua. Phase transformation and recrystallization kinetics in space–time domain during isothermal compressions for Ti−6Al−4V analyzed by multi-field and multi-scale coupling FEM [J]. Materials & Design, 2016, 94: 523−535.

[32] MOHAPATRA S, PRASAD R, JAIN J. Temperature dependence of abnormal grain growth in pure magnesium [J]. Materials Letters, 2021, 283: 128851.

[33] NICOLAŸ A, FIORUCCI G, FRANCHET J M, CORMIER J, BOZZOLO N. Influence of strain rate on subsolvus dynamic and post-dynamic recrystallization kinetics of Inconel 718 [J]. Acta Materialia, 2019, 174: 406−417.

[34] SCHAFLER E, STEINER G, KORZNIKOVA E, KERBER M, ZEHETBAUER M J. Lattice defect investigation of ECAP-Cu by means of X-ray line profile analysis, calorimetry and electrical resistometry [J]. Materials Science and Engineering A, 2005, 410/411: 169−173.

[35] MAHAJAN S. Critique of mechanisms of formation of

deformation, annealing and growth twins: Face-centered cubic metals and alloys [J]. Scripta Materialia, 2013, 68(2): 95−99.

[36] SOUAÏ N, BOZZOLO N, NAZÉ L, CHASTEL Y, LOGÉ R. About the possibility of grain boundary engineering via hot-working in a nickel-base superalloy [J]. Scripta Materialia,

2010, 62(11): 851−854.

[37] WANG W, BRISSET F, HELBERT A L, SOLAS D, DROUELLE I, MATHON M H, BAUDIN T. Influence of stored energy on twin formation during primary recrystallization [J]. Materials Science and Engineering A, 2014, 589: 112−118.

Ni80A 高温合金等温压缩过程中低能孪晶界密度在时空域的分布及演化

赵 江[1]，权国政[1,2]，张钰清[1]，熊 威[3]

1. 重庆大学 材料科学与工程学院 重庆市先进模具智能制造重点实验室，重庆 400044；
2. 华中科技大学 材料成形与模具技术国家重点实验室，武汉 430074；
3. 清华大学 核能与新能源技术研究所 先进反应堆工程与安全教育部重点实验室
先进核能技术协同创新中心，北京 100084

摘 要：调控合金热变形中低能晶界($\Sigma3^n$孪晶界)密度是提高合金晶界相关性能的重要手段。为揭示在电热成形过程中孪晶界密度的分布、演化及其与晶粒尺寸和储能相关的内在机制，建立电−热−力多场、宏微观多尺度耦合有限元模型。一系列 Ni80A 高温合金在等温压缩过程中的模拟结果表明：在加热和保温阶段，孪晶界密度基本不变；在压缩阶段，孪晶界密度先快速增加而后倾向于降低。等温压缩样中孪晶界密度的分布在高温和中等应变速率下更加均匀。与细晶粒尺寸、高储能及高动态再结晶程度相对应的热变形参数区间有助于提高孪晶界密度。

关键词：$\Sigma3^n$孪晶界；多尺度耦合模拟；电热成形；镍基高温合金

(Edited by Wei-ping CHEN)